Journal of Alloys and Compounds 552 (2013) 88–97

Contents lists available at SciVerse ScienceDirect

Journal of Alloys and Compounds

journal homepage: www.elsevier.com/locate/jalcom

Crystallization characteristics of the Mg-rich metallic glasses in the Ca–Mg–Zn system

Y.N. Zhang [a], G.J. Rocher [a], B. Briccoli [a], D. Kevorkov [a], X.B. Liu [b], Z. Altounian [b], M. Medraj [a,*]

[a] Department of Mechanical Engineering, Concordia University, 1455 de Maisonneuve Blvd. W., Montreal, Quebec, Canada H3G 1M8
[b] Center for the Physics of Materials and the Department of Physics, McGill University, 3600 University Street, Montreal, Quebec, Canada H3A 2T8

ARTICLE INFO

Article history:
Received 29 July 2012
Received in revised form 17 October 2012
Accepted 18 October 2012
Available online 29 October 2012

Keywords:
Ca–Mg–Zn
Mg-based biocompatible metallic glass
Crystallization
X-ray diffraction
Differential scanning calorimetry
Electrical resistance

ABSTRACT

Metallic glasses in the composition range of $Ca_4Mg_{72-x}Zn_{24+x}$ ($x = 0$–12, $\Delta x = 2$) were successfully prepared using the melt-spinning technique. The crystallization characteristics of the alloys were investigated by differential scanning calorimetry (DSC), X-ray diffraction (XRD) and electrical resistance measurements. All samples show a complex crystallization process with four exothermic events. The phases resulting from each crystallization stage were identified by XRD. The crystallization was initiated at lower temperatures by the precipitation of $Mg_{51}Zn_{20}$ crystals. Mg-hcp and $Ca_{16.7}Mg_{38.2}Zn_{45.1}$ (IM1) ternary compound precipitated from the retained amorphous phase during the second crystallization event. After that, $Ca_{1.5}Mg_{55.3}Zn_{43.2}$ (IM4) ternary compound formed at higher temperatures and the crystallization event terminated via IM4 transforming to $Ca_2Mg_5Zn_{13}$ (IM3) before melting. All crystallization reactions were found to be in qualitative agreement with the equilibrium phase diagram. The activation energy for each stage of crystallization was determined from DSC analysis and calculated by Kissinger method. The temperature dependence of electrical resistance shows good consistency with DSC and XRD results.

1. Introduction

The growing need for lightweight, energy-efficient, environmentally friendly products is driving the development of magnesium-based alloys [1–4]. The addition of Ca and Zn in Mg alloys enhances the castability, strength, fracture toughness, creep resistance, corrosion resistance and age hardening response [5–10]. In addition, Zn was found to increase the peak-hardness value and enhance the age hardening kinetics of Mg-Ca alloys due to the formation of ternary precipitates [6] that have lower lattice mismatch with the Mg solid solution matrix. This resulted in the refinement and uniform distribution of these precipitates along with enhanced nucleation rate in these Zn containing alloys. Furthermore, tensile and creep properties can also be further improved by adding rare earth elements to the Ca–Mg–Zn based alloys [9].

Crystalline magnesium alloys exhibit a high specific strength and are therefore an interesting material for lightweight applications. However, significant increase in yield strength can be achieved by Mg-based glasses: the absence of a dislocation-based plastic deformation mechanism in metallic glasses generates much higher yield strength and elastic strain limit than those of their crystalline counterparts [11–13]. In addition, with the absence of work-hardening, metallic glasses often show plastic flow and a tendency towards work-softening that leads to shear localization [12]. Under tensile condition, the localized accumulation of plastic flow into shear bands limits dramatically the overall plasticity, such that metallic glass specimens usually fail on one dominant shear band. This adverse property was mitigated by the development of composites containing ductile crystals in a metallic matrix [14]. Fan and Inoue's group [15] obtained nanocomposites with improved plasticity ranging up to 2.5% in compression by annealing of glassy precursor alloys. Therefore, studying the phase evolution during annealing is important for understanding the mechanical properties of these nanocomposites.

Knowledge on glass formation is important to understanding both the thermodynamic and kinetic aspects of crystallization. One of the key parameters for the glass-forming ability (GFA) of metallic liquids is the ratio between the glass transition temperature, T_g, and the liquidus temperature, T_{liq}, which is commonly referred to as the reduced glass transition temperature T_{rg} [16]. Metallic glasses are often multicomponent alloys, since addition of specific elements decreases the liquidus temperature and thus improves glass formation by increasing T_{rg}. Furthermore, the addition of elements that is chemically and topologically different from the initial species (in atomic size and valence) frustrates crystal formation [11]. The complexity and size difference of the unit cell in higher-order crystal structures progressively decrease the energetic advantage of forming a periodically ordered structure. As a frozen supercooled liquid, metallic glass compositions are not lim-

* Corresponding author.
E-mail address: mmedraj@encs.concordia.ca (M. Medraj).

0925-8388/$ - see front matter © 2012 Elsevier B.V. All rights reserved.
http://dx.doi.org/10.1016/j.jallcom.2012.10.089

ited by the interstitial solubility limit. Hence a wide range of alloy compositions can be synthesized. The nature of such metallic glasses and their ability to achieve compositions unattainable by traditional crystalline processing routes may potentially allow for superior corrosion resistance and mechanical properties.

The high elastic strain limit of metallic glasses combined with a high yield strength, fracture toughness and wear resistance makes metallic glasses suitable for high-performance springs, sporting goods, electronic products, surgical instrument, implants for bone replacement and other medical devices [12,17]. Recently, biocompatible glassy alloys with small amount of Ca have been found in the Ca–Mg–Zn ternary system for the development of biodegradable implants [13–21]. These biodegradable metallic implants can be designed to stabilize a structure by allowing bone to grow while simultaneously dissolving harmlessly in the body and thereby reducing the burden of additional surgical intervention [13,19,20]. Zberg et al. [13] also reported that Ca–Mg–Zn metallic glasses exhibit much more passive corrosion characteristics when the Zn concentration is greater than 28 at.% due to the formation and stabilization of a ZnO surface layer. Furthermore, the improvement of the corrosion resistance can be achieved by enhancing the glass-forming ability and stability for metallic glasses.

Hence the Ca–Mg–Zn system is promising as a next-generation material in both industrial and biomedical applications. Knowledge of the equilibrium and non-equilibrium phases that exist in this system is the first and essential step for further tuning the microstructures, mechanical properties and bio-corrosion resistance. To date, the Ca–Mg–Zn isothermal section at 608 K was constructed using a combination of the high-throughput diffusion couples technique and selected equilibrated key alloys [22]. A partial Ca–Mg–Zn isothermal section at 335 °C is shown in Fig. 1. Many researchers have studied the $Ca_2Mg_6Zn_3$ compound, but their results are contradictory [23–28]. More recently, the solubility range and crystal structure of a Mg-rich solid solution $Ca_3Mg_xZn_{15-x}$ ($4.6 \leqslant x \leqslant 12$ at 608 K), IM1 (intermetallic compound), were determined using scanning electron microscopy (SEM), electron probe micro-analysis (EPMA), transmission electron microscopy (TEM) and x-ray diffraction (XRD) by our group [29]. In addition, the crystallographic information and homogeneity range of another ternary solid solution $Ca_2Mg_5Zn_{13}$ (IM3), determined by SEM, EPMA, EBSD, TEM and X-ray diffraction, were reported by our group [30]. Furthermore, the most promising compositions to produce bulk metallic glass on the Mg–Zn side was reported by Ma and Xu [19], where the compositions contain 4 at.% of Ca. Therefore, the aims of this research are: (1) finding the composition having the best glass-forming ability and stability in the $Ca_4Mg_{72-x}Zn_{24+x}$ ($x = 0–12$, $\Delta x = 2$) composition range; (2) studying the crystallization characteristics of the Ca–Mg–Zn metallic glasses using XRD, DSC and resistance measurements. The results of the above $Ca_4Mg_{72-x}Zn_{24+x}$ metallic glass characteristics will be applied for further studies on the mechanical properties and bio-corrosion resistant characteristics.

2. Experimental procedures

Six key alloys were prepared. The starting materials were supplied by Alfa Aesar with purities of 99.98% Mg, 99.99% Zn and 99% Ca. The key alloys were prepared in an arc-melting furnace with water-cooled copper crucible under an argon atmosphere using a non-consumable tungsten electrode. Samples were remelted five times to ensure homogeneity. To compensate for the mass loss of Mg and Zn due to their high vapor pressure, extra 8 and 12 weight percentages of Mg and Zn, respectively, were added to the compositions before melting. The samples were then crushed into appropriate sizes for single-roller melt-spinning. The melt-spinning was carried out under helium at a pressure of 50 kPa with a wheel tangential speed of 30 m/s. The resulting ribbons were approximately 2 mm wide and 30 μm thick. The actual composition of the ribbon samples was determined by Inductively Coupled Plasma (ICP), as shown in Fig. 1. The difference between nominal compositions and actual compositions is below 3 at.%. The actual compositions were used for the analysis.

XRD was used to verify the amorphous state on the free side of each ribbon and to characterize the samples after each exothermic crystallization peak. The XRD patterns were obtained using PANalytical X'pert Pro powder X-ray diffractometer with a CuKα radiation at 45 kV and 40 mA. The XRD spectrum was acquired from 20° to 120° 2θ with a 0.02° step size and 2 s of a point scan time. The analysis of the X-ray patterns was carried out using X'Pert HighScore Plus Rietveld analysis software in combination with Pearson's crystal database [31].

The thermal stability, glass transition, crystallization temperatures and crystallization kinetics of the as-quenched glassy samples were studied by means of calibrated non-isothermal DSC from SETARAM Instrumentation under a continuous flow of purified argon. Samples were placed in a graphite crucible and covered with a lid. To determine the activation energy for crystallization, samples were heated at rates of 5, 10, 20 and 40 K/min to 673 K and subsequently cooled to room temperature at a constant cooling rate of 40 K/min. After each exothermic peak, the samples were investigated by XRD to characterize the products after each crystallization event.

The changes in electrical resistance from room temperature to 623 K were measured on 2 mm wide and 100 mm long rectangular shaped ribbon samples by the conventional four-probe technique in an argon filled resistance furnace, where the voltage was measured using a Keithley 2182A nanovoltmeter and a constant 50 mA current was provided by a Thurlby Thandar PL-303 power supply. A thermocouple with ±2 °C accuracy was placed under the sample to record its temperature. A heating rate of 5 K/min was used to compare the thermal behavior with that obtained using DSC. 1 K/min heating rate was applied for samples with more Zn concentrations $Ca_4Mg_{72-x}Zn_{24+x}$ ($x \geqslant 8$) to slightly reduce the onset temperature of the last crystallization event, which enabled to obtain the results before melting the samples.

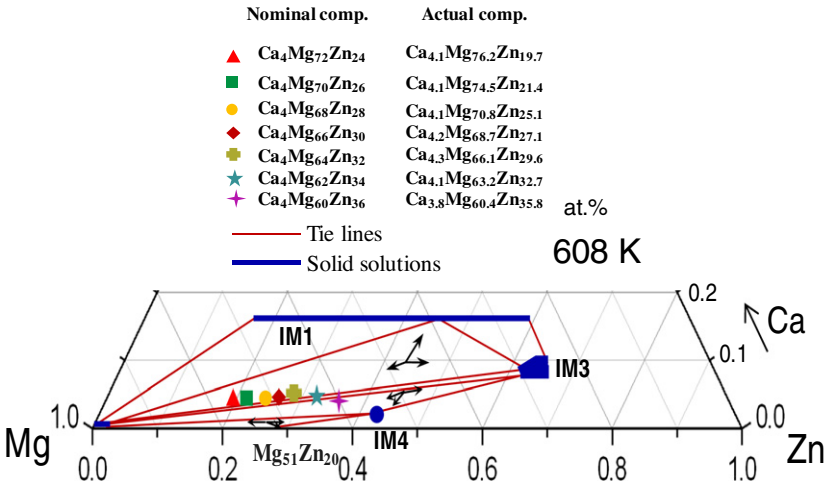

Fig. 1. Partial isothermal section of the Mg–Zn–Ca system at 608 K [22]. The actual compositions of the glassy samples are shown on the phase diagram. Three-phase regions are marked by arrows.

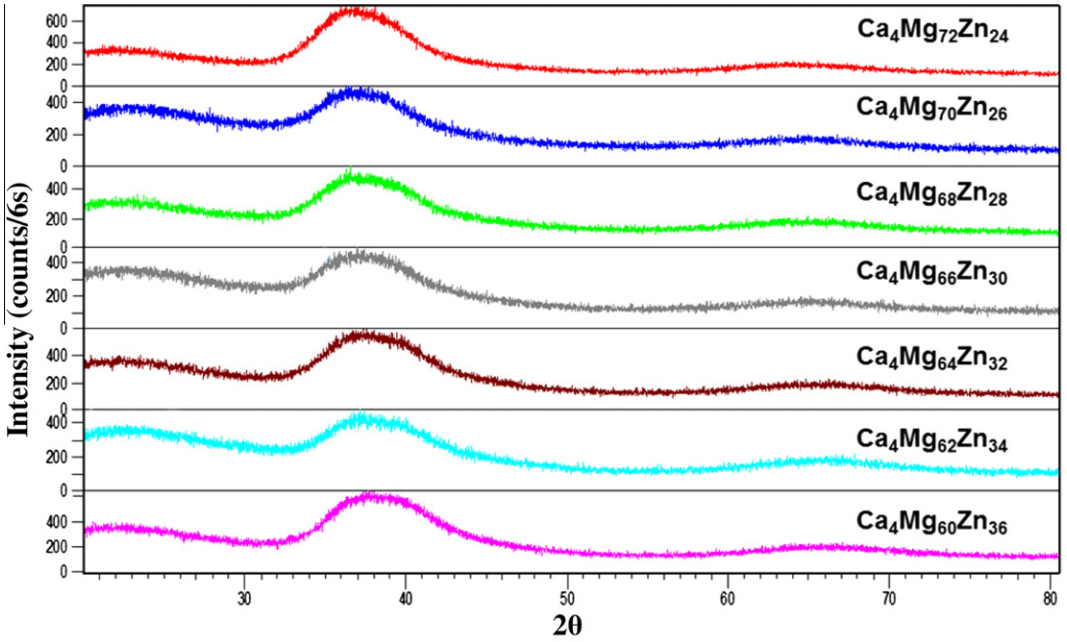

Fig. 2. XRD patterns obtained from the free side of the as-quenched Ca–Mg–Zn metallic glasses with the $Ca_4Mg_{72-x}Zn_{24+x}$ compositions.

3. Results and discussion

Fig. 2 shows the XRD patterns obtained from the free side of the as-quenched Ca–Mg–Zn metallic glasses with the compositions of $Ca_4Mg_{72-x}Zn_{24+x}$. The absence of detectable crystalline diffraction peaks, together with the broad scattering peaks around 37° and 67°, confirmed the amorphous nature of these samples. With increasing Zn content, the broad scattering maxima shift slightly towards higher diffraction angles due to the fact that Zn atoms have a smaller atomic radius than Mg atoms.

3.1. Glass transition, crystallization and activation studies by DSC

Fig. 3 presents the DSC curves obtained at a constant heating rate of 5 K/min showing the glass transition, four crystallization events (marked by T_{p1}, T_{p2}, T_{p3} and T_{p4}) and one melting event of the Ca–Mg–Zn metallic glasses. For this series of alloys with constant Ca content, the glass transition temperature (T_g) and the peak temperature of glass transition (T_g peak) do not show significant variation with composition, as shown in Fig. 4(a). The first crystallization temperature (T_{x1}), the peak temperature of the first crystallization (T_{p1}) as well as the width of the supercooled liquid region ($\Delta T_x = T_{x1} - T_g$) or ($\Delta T_x$ peak $= T_{p1} - T_g$ peak) increase monotonically with decreasing Mg content. The melting temperature (T_l) changes with varying compositions. When x approaches 6, the melting shoulder shrinks, giving the lowest melting temperature in these samples, as shown in Fig. 4(a) with the actual compositions. Fig. 4(b) represents the composition dependence of the reduced glass transition temperature ($T_{rg} = T_g/T_l$) with the actual compositions for $Ca_4Mg_{72-x}Zn_{24+x}$ metallic glasses. The "strong liquid" behavior of metallic glasses results in a reduced rate of both crystal nucleation and growth, and therefore contributes greatly to

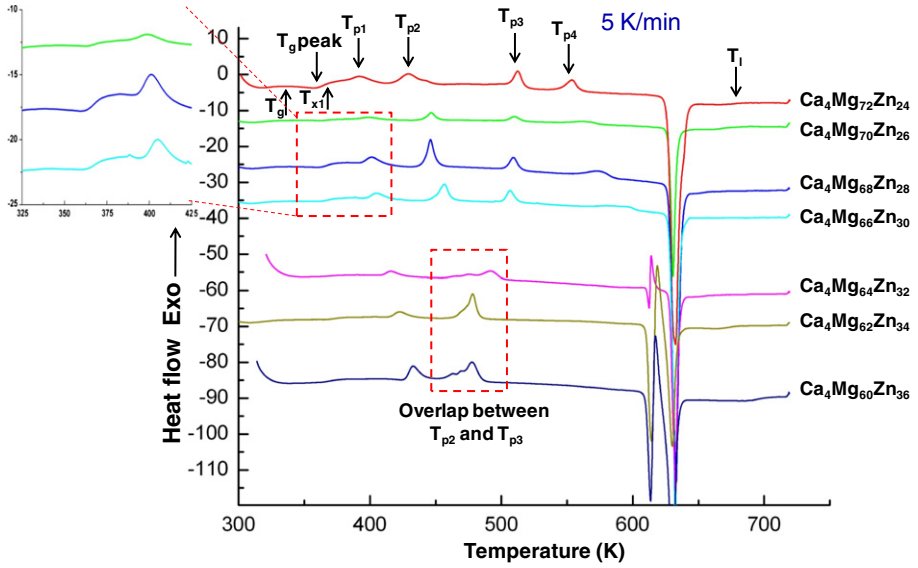

Fig. 3. DSC curves measured at a constant heating rate of 5 K/min showing the glass transition, crystallization and melting behavior of the $Ca_4Mg_{72-x}Zn_{24+x}$ metallic glasses.

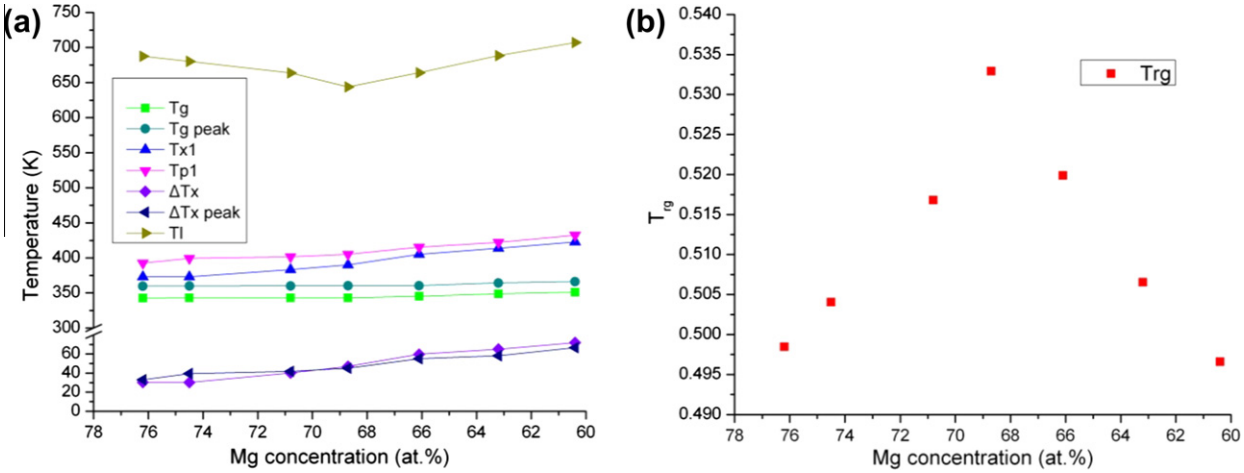

Fig. 4. Composition dependence of characteristic temperatures (a) (T_g, T_g peak, T_{x1}, T_{p1}, ΔT_x, ΔT_x peak and T_l) and (b) T_{rg} of the $Ca_4Mg_{72-x}Zn_{24+x}$ metallic glasses with the actual compositions obtained at a constant heating rate of 5 K/min.

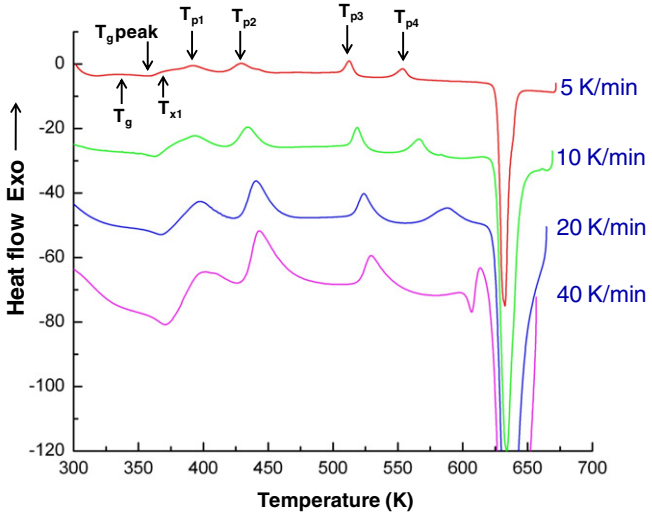

Fig. 5. The DSC curves of the Ca–Mg–Zn metallic glass with the $Ca_4Mg_{72}Zn_{24}$ composition at 5, 10, 20 and 40 K/min heating rates.

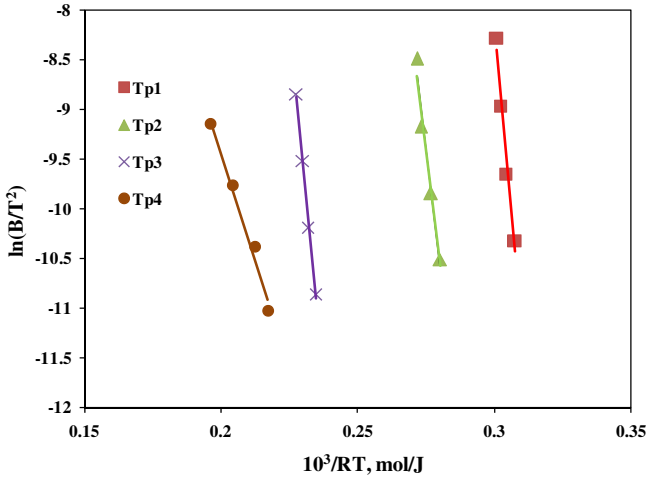

Fig. 6. Kissinger plots of $\ln(B/T^2)$ versus $1/RT$ obtained from heating cycles of the DSC curves for the $Ca_4Mg_{72}Zn_{24}$ composition.

Table 1
Characteristic temperature and activation energies for the crystallization events of the $Ca_4Mg_{72}Zn_{24}$ metallic glass: four crystallization peak temperatures (T_{p1}, T_{p2}, T_{p3}, and T_{p4}) and activation energies (E_{x1}, E_{p1}, E_{p2}, E_{p3}, and E_{p4}).

Heating rate [K min^{-1}]	T_{p1} [K]	T_{p2} [K]	T_{p3} [K]	T_{p4} [K]
5	391.3	429.5	512.5	554
10	395.4	434.7	518.6	566.5
20	397.9	440.4	523.6	589.4
40	400.2	442.7	529.1	613.7
Activation energies [kJ mol^{-1}]	300 ± 16	230 ± 14	276 ± 5	86 ± 4

the extraordinary glass-forming ability [12]. The maximum T_{rg} was found to be 0.53 at an actual composition close to $Ca_{4.2}Mg_{68.7}Zn_{27.1}$, resulting in the best GFA, conforming to the literature [19].

Fig. 5 shows the DSC curves of the $Ca_4Mg_{72}Zn_{24}$ metallic glass at various heating rates of 5, 10, 20 and 40 K/min. It is clear that T_g, T_{x1} and the exothermic crystallization peak temperatures (T_p), shift to higher temperatures with increased heating rate. The crystallization events are heating rate dependent, indicating that the nucleation and phase transformation are thermally activated processes. Whereas the rate dependence of the kinetic glass transition temperature (T_g) is due to the relaxation process in the glass transition region [32,33]. The apparent activation energy of each characteristic transformation was evaluated by Kissinger method [34]. The Kissinger Eq. (1) is based on the shift of the DSC curves with respect to different heating rates:

$$\ln(B/T^2) = -E/RT + C \quad (1)$$

where E is the apparent activation energy, B is the heating rate, R is the gas constant, C is a constant and T is the characteristic temperature such as T_{p1}, T_{p2}, T_{p3} and T_{p4} indicated on the DSC curves.

As an example, the Kissinger plots for $Ca_4Mg_{72}Zn_{24}$ are shown in Fig. 6. The corresponding values of the characteristic temperatures and calculated activation energies are listed in Table 1. The variation in activation energies for all actual compositions is shown in Fig. 7. As demonstrated in Fig. 7, the 1st crystallization peak temperature T_{p1} is sensitive to composition where most of the amorphous phase changes into the $Mg_{51}Zn_{20}$ intermetallic phase. In contrast, the 2nd crystallization peak temperature T_{p2} is relatively less sensitive to composition. The activation energy of the 1st crystallization E_{p1} is higher than the others due to transformation from amorphous to crystalline materials at this step, whereas the other steps include growth of nuclei. In addition, the values of E_{p1} are higher for the compositions with more Mg concentration, Ca_{4-}

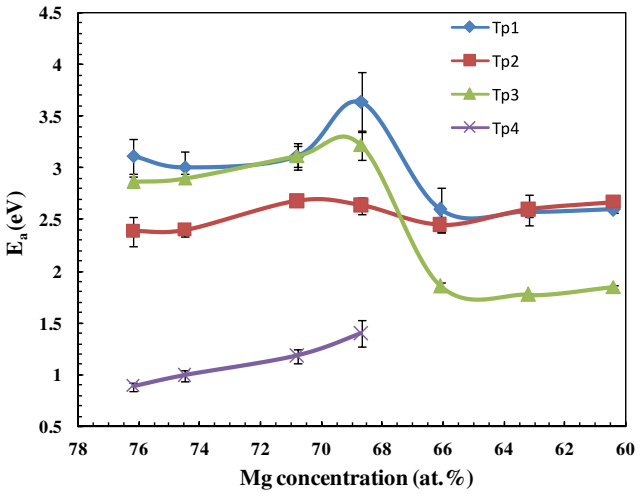

Fig. 7. The activation energies of the four crystallization events of all the actual compositions.

$Mg_{72-x}Zn_{24+x}$ ($x \leqslant 6$), than for the compositions with more Zn concentration, $Ca_4Mg_{72-x}Zn_{24+x}$ ($x \geqslant 8$), while the apparent activation energy E_{p2} for T_{p2} is similar in all the samples. The 3rd and 4th crystallization peak temperatures, T_{p3} and T_{p4}, are sensitive to composition. The apparent activation energy E_{p4} for the $Ca_4Mg_{72-x}Zn_{24+x}$ ($x \geqslant 8$) compositions was not possible to calculate due to the overlap between the crystallization reaction and the sample melting. The activation energy E_{p3} and E_{p4} are much less important than each of the previous energy terms E_{p1} and E_{p2} from a crystallization point of view. This is because crystallization has already taken place to a readily detectable extent at T_{p2} (see Fig. 9 obtained by XRD) and only a negligible amount of amorphous phase is present at this point. In addition, in most applications, the processing temperature should not exceed T_{p1} in order to keep the amorphous nature and prevent intermetallic phases from forming and growing. The apparent activation energy consists of nucleation and crystal growth [35,36]. It is a measure of the thermodynamic barrier to crystallization. Higher crystallization activation energies generally favor thermal stability. The higher activation energies E_{p1} suggest that compositions with more Mg concentrations, $Ca_4Mg_{72-x}Zn_{24+x}$ ($x = 0$–6, $\Delta x = 2$), should have higher resistance or better thermal stability against crystallization than compositions with more Zn concentration, $Ca_4Mg_{72-x}Zn_{24+x}$ ($x = 8$–12, $\Delta x = 2$). The maximum E_{p1} obtained for the $Ca_{4.2}Mg_{68.7}Zn_{27.1}$ actual composition shows the best thermal stability compared to other samples. This is consistent with the results (Fig. 4b) obtained from the reduced glass transition temperature T_{rg}, which shows that a metallic glass with a higher glass-forming ability tend to show better thermal stability due to their more efficient and stable atomic packing in local structures.

3.2. Crystallization characteristics by XRD

The Ca–Mg–Zn as-quenched glassy samples were heated at a rate of 5 K/min just above their respective peak temperature and cooled rapidly to room temperature with a continuous argon gas flow without isothermal holding. XRD was used to characterize the crystallization of each peak. Full pattern refinement was

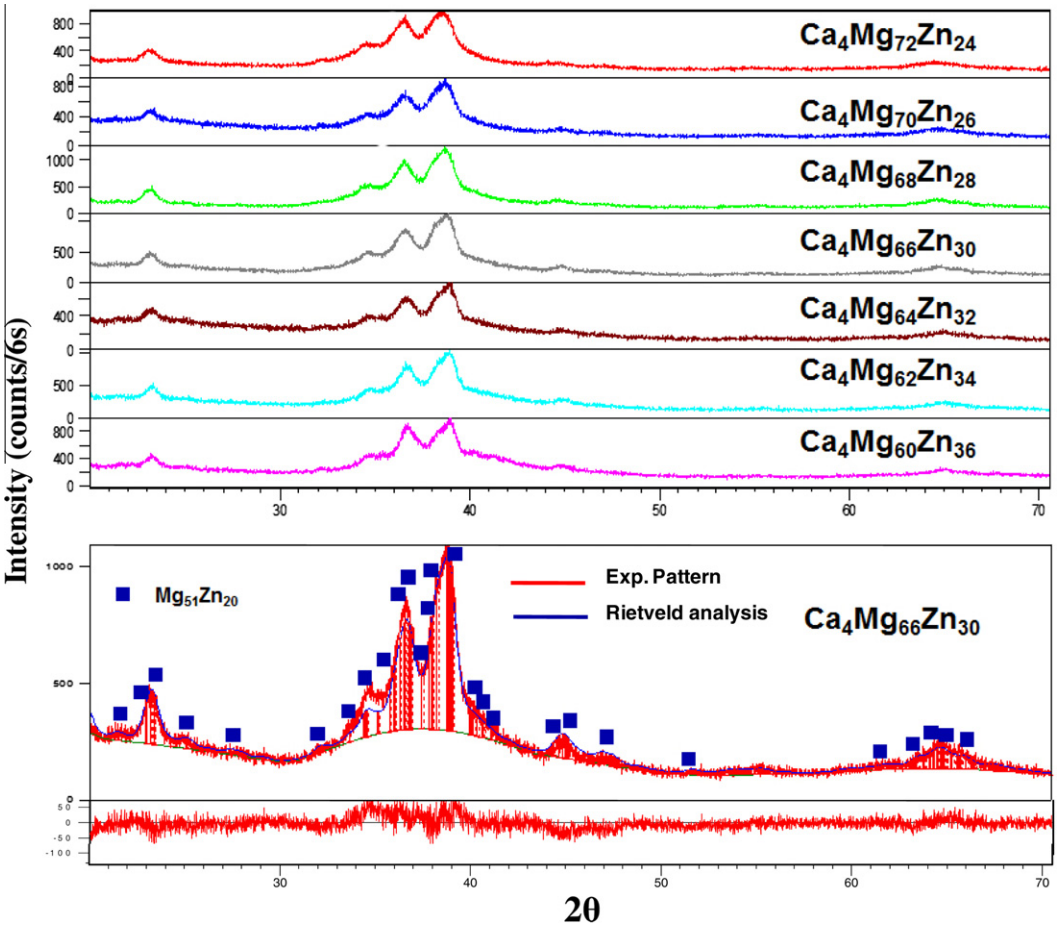

Fig. 8. XRD Rietveld analysis for the $Ca_4Mg_{72-x}Zn_{24+x}$ compositions heated beyond the 1st crystallization temperature at 5 K/min showing the $Mg_{51}Zn_{20}$ binary compound and the presence of retained amorphous phase.

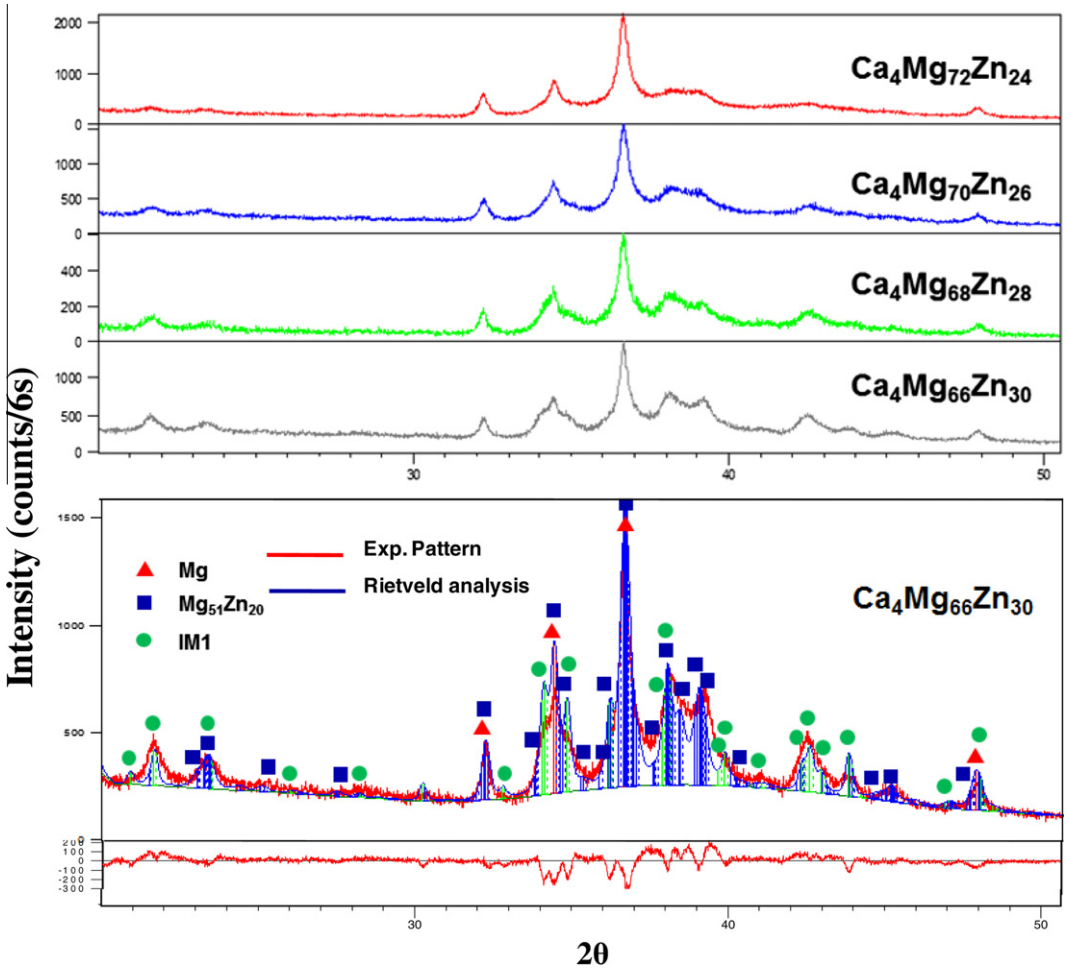

Fig. 9. XRD Rietveld analysis for the $Ca_4Mg_{72-x}Zn_{24+x}$ ($x \leqslant 6$) compositions heated beyond the 2nd crystallization temperature at 5 K/min showing the formation of $Mg_{51}Zn_{20}$, Mg and IM1.

carried out by the Rietveld method for all the compositions, as shown in Figs. 8–11. Since the $Ca_4Mg_{66}Zn_{30}$ composition has shown the best glass-forming ability, it is used as an example for Rietveld analysis at the bottom of each of these figures. The differences between the calculated and the experimental XRD patterns were also presented in the figures. The crystallographic parameters of the refined phases for each crystallization process are presented in Table 2. For the refinement, the atomic coordinates and site occupancy of IM1 and IM3 ternary compounds were taken from our previous findings [29,30].

XRD Rietveld analysis (Fig. 8) shows that after heating the samples beyond the 1st crystallization temperature (T_{p1}) around 423 K, $Mg_{51}Zn_{20}$ crystals precipitate but a significant amount of the amorphous phase still remains. The result shows a good consistency with the binary Mg–Zn metallic glass from $Mg_{80}Zn_{20}$ to $Mg_{60}Zn_{40}$ [37] where $Mg_{51}Zn_{20}$ binary compound also formed during first crystallization peak. However, the obtained lattice parameters of the $Mg_{51}Zn_{20}$ binary compound (Table 1) are larger than these observed in the binary system. This is due to the larger Ca atom present in the $Mg_{51}Zn_{20}$ solid solution. No peak shift of the $Mg_{51}Zn_{20}$ compound was noticed for all the compositions of $Ca_4Mg_{72-x}Zn_{24+x}$. Therefore, Ca concentration was the same in the $Mg_{51}Zn_{20}$ solid solution for all compositions.

Mg and the $Ca_{16.7}Mg_{38.2}Zn_{45.1}$ (IM1) ternary compound precipitate from the remaining amorphous phase in the 2nd crystallization event of the $Ca_4Mg_{72-x}Zn_{24+x}$ ($x \leqslant 6$) compositions at around 483 K, as shown in Fig. 9. It is very clear that with increasing the Zn concentration, more IM1 ternary compound forms, which is consistent with the Ca–Mg–Zn ternary phase diagram [22]. In addition, the lattice parameters of the $Mg_{51}Zn_{20}$ compound formed after the 2nd crystallization temperature (T_{p2}) decrease compared with those formed during the 1st crystallization peak (T_{p1}), as illustrated in Table 1. Thus, less Ca is dissolved in the $Mg_{51}Zn_{20}$ solid solution after the 2nd crystallization process, indicating that these Ca atoms were used to form the stable IM1 ternary compound. As the second and third exothermic reactions in the $Ca_4Mg_{72-x}Zn_{24+x}$ ($x \geqslant 8$) compositions are overlapping (Fig. 3), it is very difficult to separate their effect and obtain the phase formation after these peaks by XRD.

Mg, IM1 and $Ca_{1.5}Mg_{55.3}Zn_{43.2}$ (IM4) form at a higher temperature (around 533 K) during the 3rd crystallization event (Fig. 3) for all the compositions, as shown in Fig. 10. Although the crystal structure of IM4 was not fully resolved in terms of the space group and prototype, the composition and XRD patterns were determined at 608 K in our previous work [22]. However, the Rietveld analysis was not applied for IM4 due to the incomplete crystallographic information. With increasing Zn concentration, the intensities of the IM4 peaks increase, such as the peak at 37°–38° 2θ. However, the intensities of Mg and IM1 peaks and their lattice parameters do not change significantly. This is because these compounds have stabilized after the previous crystallization event (T_{p2}).

The crystallization event terminated after the 4th exothermic reaction by IM4 transforming to $Ca_2Mg_5Zn_{13}$ (IM3) before melting. XRD Rietveld analysis for the compositions of $Ca_4Mg_{72-x}Zn_{24+x}$ ($x \leqslant 6$) at 5 K/min heating rate and $Ca_4Mg_{72-x}Zn_{24+x}$ ($x \geqslant 8$) at

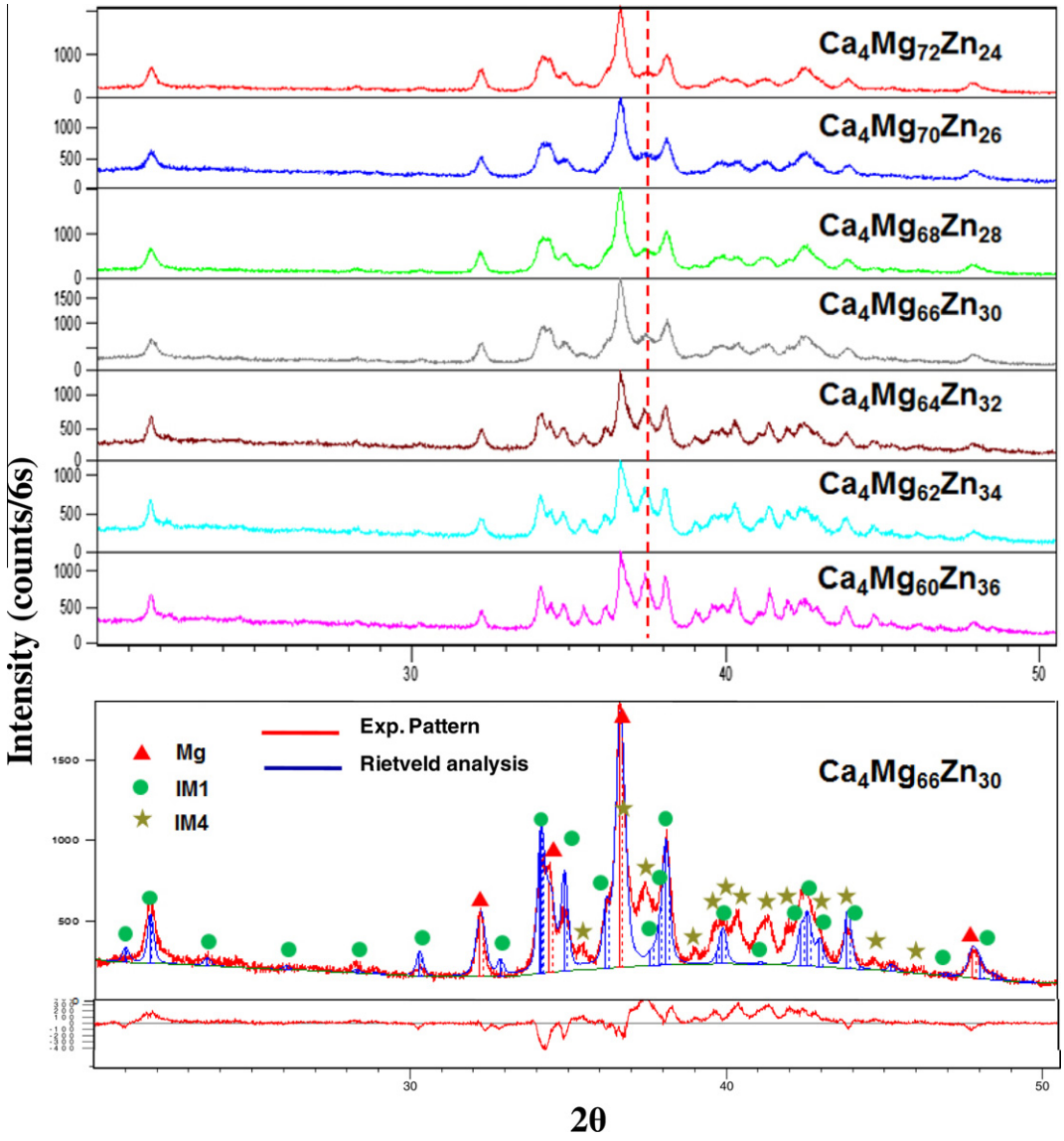

Fig. 10. XRD Rietveld analysis for the $Ca_4Mg_{72-x}Zn_{24+x}$ compositions heated beyond the 3rd crystallization temperature at 5 K/min showing the formation of Mg, IM1 and IM4.

1 K/min heating rate heated beyond the crystallization temperature of the 4th peak at around 593 K is shown in Fig. 11. The 1 K/min heating rate was used for $Ca_4Mg_{72-x}Zn_{24+x}$ ($x \geqslant 8$) to obtain the final crystallization event while avoiding sample melting. Fig. 11 demonstrates the Rietveld analysis for the Mg + IM1 + IM3 compounds in the samples. The lattice parameters of Mg in the samples do not show significant differences compared to the parameters after the 2nd and the 3rd peak, whereas the lattice parameters of IM1 increased slightly to a(Å) = 9.474 and c(Å) = 9.961, which corresponds to the composition of $Ca_{16.7}Mg_{38.2}Zn_{45.1}$. In addition, the lattice parameters of IM3 are close to the composition of $Ca_{8.8}Mg_{30.1}Zn_{61.1}$. These compositions are consistent with the phase relationship among the Mg, IM1 and IM3 compound in the Ca–Mg–Zn phase diagram. Furthermore, all the crystallization products were shown to be in qualitative agreement with the equilibrium phase diagram [22].

3.3. Crystallization characteristics by electrical resistance

All the samples in the composition range of $Ca_4Mg_{72-x}Zn_{24+x}$ exhibit numerous changes in the temperature coefficient of resistance (TCR), $\alpha = dR/RdT$, over the whole temperature range, as can be seen in Fig. 12. The TCR results with various slope changes show a good consistency with the DSC curves measured at a constant heating rate of 5 K/min (Fig. 3) in terms of glass transition and crystallization events. All compositions show clear changes of TCR from negative to positive at T_g (around 358 K), which is in accordance with the change from amorphous state to supercooled liquid state [38,39]. Subsequently, as typically expected for crystallization at around 398 K, the resistance first decreases slightly then rapidly decreases resulting in a TCR change from positive to negative [37]. On one hand, the four Mg-rich samples with the $Ca_4Mg_{72-x}Zn_{24+x}$ ($x \leqslant 6$) compositions undergo four crystallization steps: (I) $Mg_{51}Zn_{20}$ + amorphous, then (II) Mg + $Mg_{51}Zn_{20}$ + IM1, followed by two more crystallization and grain growth events consisting of (III) Mg + IM1 + IM4 and finally (IV) the Mg + IM1 + IM3 equilibrium phases. On the other hand, the three samples with more Zn concentration ($Ca_4Mg_{72-x}Zn_{24+x}$ ($x \geqslant 8$) compositions) show different features where the (II) and (III) crystallization events overlap, resulting in similar slope but two different phase transformation: First crystallization event: $Mg_{51}Zn_{20}$ + amorphous → $Mg_{51}Zn_{20}$ + Mg + IM1; Second crystallization event: $Mg_{51}Zn_{20}$ + Mg + IM1 → Mg + IM1 + IM4. As shown by XRD after the (III) crystallization event, all samples have the Mg + IM1 + IM4

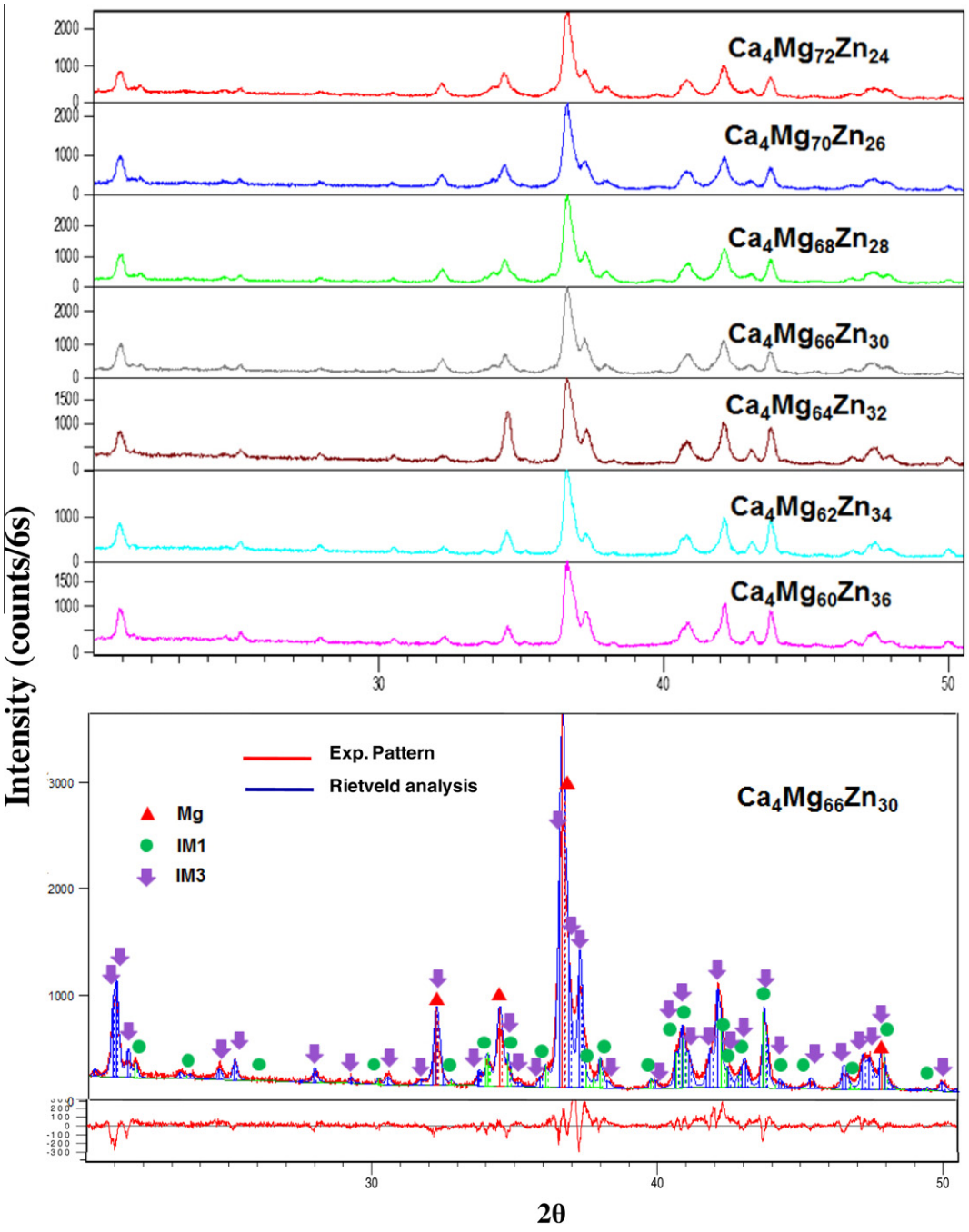

Fig. 11. XRD Rietveld analysis for the $Ca_4Mg_{72-x}Zn_{24+x}$ compositions heated beyond the 4th crystallization temperature at 5 K/min showing Mg, IM1 and IM3.

phases as demonstrated in Fig. 10. At 573 K for Zn-rich samples, the heating rate for the electrical resistance measurement was changed to 1 K/min in order to entirely capture the final crystallization event while avoiding sample melting. All the phenomena of crystallization event obtained from electrical resistance for the samples with more Mg and those with more Zn concentrations are in an agreement with the DSC (Fig. 3) and XRD (Figs. 8–11) results in terms of the crystallization temperatures and the phase constituents after the four crystallization steps.

As anticipated, during transformations leading to increased structural ordering, TCR of all the samples remains negative throughout the crystallization steps [40]. However, a positive TCR was found between the last two crystallization events between T_{p3} and T_{p4} due to the growth of Mg, IM1 and IM4 crystals as well as to the phonon contribution to the resistance [41]. According to the XRD data acquired after the 3rd to 4th crystallization events in Figs. 10 and 11, with increasing Zn concentration in the samples, the amount of IM4 ternary compound increases, which is also detected by the difference in electrical resistance in Fig. 12. Sample $Ca_4Mg_{60}Zn_{36}$ gives the highest resistance change in the 4th crystallization events amongst all the samples. Such a large resistance change may be attributed to the complexity of the IM4 structure. During the natural convection cooling presented in dotted line at the bottom of Fig. 12, the samples with more Mg concentration have lower resistance due to the fact that Mg has a lower resistivity than Zn [37].

Table 2
The crystallographic parameters of the refined phases for each crystallization process of $Ca_4Mg_{66}Zn_{30}$.

Peak number	Phases identified by XRD	Unit cell parameters and space group			
		a [Å]	*b* [Å]	*c* [Å]	Space group
P1	$Mg_{51}Zn_{20}$	14.224	14.195	14.667	Immm
	Amorphous	–			
P2	$Mg_{51}Zn_{20}$	14.125	14.183	14.586	Immm
	Mg	3.205	3.205	5.210	$P6_3/mmc$
	IM1	9.459	9.459	9.926	$P6_3/mmc$
P3	Mg	3.206	3.206	5.206	$P6_3/mmc$
	IM1	9.438	9.438	9.916	$P6_3/mmc$
	IM4	–			
P4	Mg	3.207	3.207	5.207	$P6_3/mmc$
	IM1	9.474	9.474	9.961	$P6_3/mmc$
	IM3	14.748	14.748	8.783	$P6_3/mmc$

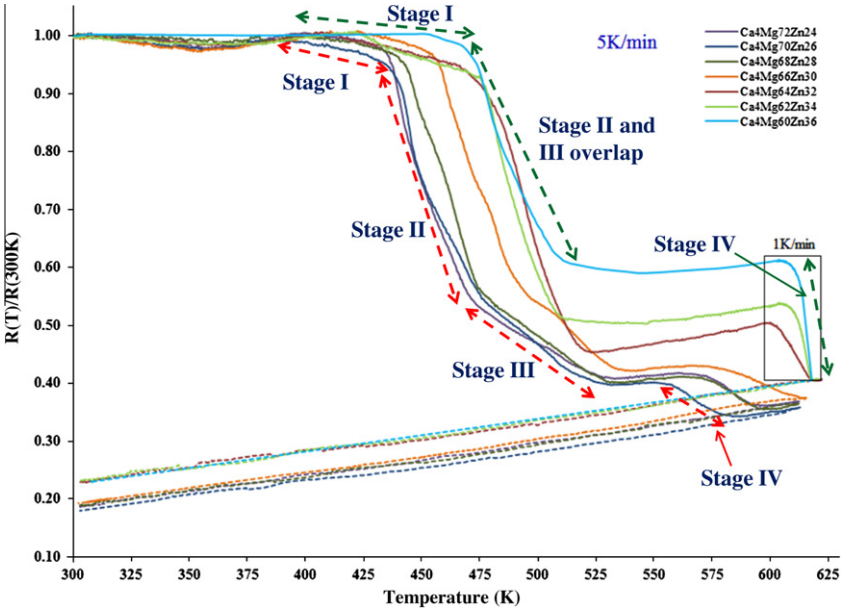

Fig. 12. The change of electrical resistance for the $Ca_4Mg_{72-x}Zn_{24+x}$ metallic glasses with temperature at a constant heating rate of 5 K/min, normalized to the value at 300 K.

4. Conclusions

The crystallization characteristics of the Ca–Mg–Zn metallic glasses were studied using DSC, XRD and electrical resistance. All samples show a complex crystallization process taking place through four exothermic reactions. The glass transition, crystallization and activation energy were studied by DSC. The activation energy for each stage of crystallization was determined from DSC analysis and calculated using Kissinger method. The maximum T_{rg} and E_{p1} obtained for the $Ca_{4.2}Mg_{68.7}Zn_{27.1}$ composition show the best glass-forming ability and thermal stability compared to other samples. The phases resulting from each crystallization stage were identified by Rietveld analysis. The crystallization of amorphous Ca–Mg–Zn metallic glasses initiated at lower temperatures (390 to 400 °C) by the precipitation of $Mg_{51}Zn_{20}$ crystals. Mg and IM1 ternary compound then precipitated from the remaining amorphous phase during the second crystallization event. At higher temperatures Mg + IM1 + IM4 formed. Finally, the crystallization event ended with the formation of Mg + IM1 + IM3 before melting. All crystallization products are in agreement with the equilibrium phase diagram. The change in electrical resistance shows a good consistency with the glass transitions and crystallization processes measured by DSC and XRD, respectively.

Acknowledgments

The authors would like to thank Xue Dong (David) Liu of the Physics Department of McGill University for useful discussions and suggestions.

References

[1] T.M. Pollock, Science 328 (2010) 986–987.
[2] A.A. Luo, Int. Mater. Rev. 49 (2004) 13–30.
[3] J.F. Wang, S. Gao, P.F. Song, X.F. Huang, Z.Z. Shi, F.S. Pan, J. Alloys Comp. 509 (2011) 8567–8572.
[4] T. Zhou, H. Xia, M.B. Yang, Z.M. Zhou, K. Chen, J.J. Hu, Z.H. Chen, J. Alloys Comp. 509 (2011) L145–L149.
[5] M. Aljarrah, M. Medraj, X. Wang, E. Essadiqi, G. Dénès, A. Muntasar, J. Alloys Comp. 438 (2007) 131–141.
[6] F. Nie, B.C. Muddle, Scr. Mater. 37 (1997) 1475–1481.
[7] G. Levi, S. Avraham, A. Zilberov, M. Bamberger, Acta Mater. 54 (2006) 523–530.
[8] B. Langelier, X. Wang, S. Esmaeili, Mater. Sci. Technol. A 538 (2012) 46–251.
[9] X. Gao, S.M. Zhu, B.C. Muddle, J.F. Nie, Scr. Mater. 53 (2005) 1321–1326.
[10] M.Q. Cong, Z.Q. Li, J.S. Liu, M.Y. Yan, K. Chen, Y.D. Sun, M. Huang, C. Wang, B.P. Ding, S.L. Wang, J. Alloys Comp. 539 (2012) 168–173.
[11] W.L. Johnson, Mater. Res. Bull. 24 (1999) 42–56.
[12] J.F. Löffler, Intermetallics 11 (2003) 529–540.
[13] B. Zberg, P.J. Uggowitzer, J.F. Löffler, Nat. Mater. 8 (2009) 887–891.
[14] G. He, J. Echert, W. Loser, L. Schultz, Nat. Mater. 2 (2003) 33–37.
[15] C. Fan, C. Li, A. Inoue, Phys. Rev. B 51 (2000) 3763–3782.

[16] D. Turnbull, Metall. Mater. Trans. B 12 (1981) 217–230.
[17] O. Buchanan, Mater. Res. Bull. 27 (2002) 850–851.
[18] B. Zberg, E.R. Arataa, P.J. Uggowitzera, J.F. Löffler, Acta Mater. 57 (2009) 3223–3231.
[19] E. Ma, J. Xu, Nat. Mater. 8 (2009) 855–857.
[20] X.N. Gu, Y.F. Zheng, S.P. Zhong, T.F. Xi, J.Q. Wang, W.H. Wang, Biomaterials 31 (2010) 1093–1103.
[21] Y.Y. Zhao, X. Zhao, J. Alloys Comp. 515 (2012) 154–160.
[22] Y.N. Zhang, D. Kevorkov, F. Bridier, M. Medraj, Sci. Technol. Adv. Mater. 12 (2011) 025003.
[23] R. Paris, Ministère de L'Air 45 (1934) 1–86.
[24] J.B. Clark, Trans. AIME 221 (1961) 644–645.
[25] J.B. Clark, Joint Committee on Powder Diffraction Standards (JCPDS) Card (1961) 12–0266.
[26] T.V. Larinova, W.W. Park, B.S. You, Scr. Mater. 45 (2001) 7–12.
[27] P.M. Jardim, G. Solorzano, J.B.V. Sande, Microsc. Microanal. 8 (2002) 487–496.
[28] K. Oh-ishi, R. Watanabe, C.L. Mendis, K. Hono, Mater. Sci. Technol. A 526 (2009) 177–184.
[29] Y.N. Zhang, D. Kevorkov, J. Li, E. Essadiqi, M. Medraj, Intermetallics 18 (2010) 2402–2411.
[30] Y.N. Zhang, D. Kevorkov, X.D. Liu, F. Bridier, P. Chartrand, M. Medraj, J. Alloys Comp. 523 (2012) 75–82.
[31] P. Villars, K. Cenzual, Pearson's Crystal Data, 2010.
[32] R. Busch, Y.J. Kim, W.L. Johnson, J. Appl. Phys. 77 (1995) 4039–4043.
[33] X. Ou, G.Q. Zhang, X. Xu, L.N. Wang, J.F. Liu, J.Z. Jiang, J. Alloys Comp. 441 (2007) 181–184.
[34] H.E. Kissinger, Anal. Chem. 29 (1957) 1702–1706.
[35] X.P. Li, M. Yan, B.J. Yang, J.Q. Wang, G.B. Schaffer, M. Qian, Mater. Sci. Technol. A 530 (2011) 432–439.
[36] Z.Z. Yuan, X.D. Chen, B.X. Wang, Y.J. Wang, J. Alloys Comp. 407 (2006) 163–169.
[37] Z. Altounian, Tu Guo-Hua, J.O. Strom-Olsen, J. Mater. Sci. 17 (1982) 3268–3274.
[38] J. Guo, F.Q. Zu, Z.H. Chen, X.F. Li, Y. Xi, R.R. Shen, Y. Zhang, J. Non-Cryst. Solids 352 (2006) 3859–3863.
[39] O. Haruyama, N. Annoshita, H. Kimura, N. Nishiyama, A. Inoue, J. Non-Cryst. Solids 312–314 (2002) 552–556.
[40] K. Pekala, R. Trykozko, J. Ostatek, H. Matyja, Appl. Phys. 22 (1980) 369–372.
[41] B.K. Park, J.H. Lee, D.Y. Kim, N.M. Hwang, J. Am. Ceram. Soc. 84 (2001) 2707–2709.